X-raying Abell 2125: a Rich Cluster of Galaxies in its Infancy

Q. Daniel Wang[1], Frazer Owen,[2] and Michael Ledlow[3]

ABSTRACT

We present an 82 ksec *Chandra* ACIS-I observation of a large-scale hierarchical complex, which consists of various clusters/groups of galaxies and low-surface brightness emission at $z = 0.247$. This high-resolution *Chandra* observation allows us for the first time to separate unambiguously the X-ray contributions from discrete sources and large-scale diffuse gas. The diffuse X-ray emission around the core cluster Abell 2125 can be characterized by a thermal plasma with a characteristic temperature of $3.2^{+0.5}_{-0.4}$ keV and a heavy element abundance of $0.24^{+0.15}_{-0.12}$ solar (90% confidence uncertainties). In comparison, a patch of relatively prominent low-surface brightness X-ray emission is shown to have a significantly lower temperature of $0.98^{+0.22}_{-0.27}$ keV and an abundance of $\lesssim 0.09$. Substructure is present in diffuse X-ray-emitting gas on all scales down to the arcsecond resolution of the data and is apparently energy-dependent. In particular, soft X-ray enhancements are found to be associated with bright radio galaxies in the core of Abell 2125, indicating intense interactions between galaxies and their clustering environment. A distinct X-ray trail, for example, appears on one side of the relatively fast-moving galaxy C153, which has a highly disturbed optical morphology. The *Chandra* observation, together with extensive multi-wavelength data on the complex, offers an unprecedentedly clear view of a forming rich cluster of galaxies.

Subject headings: cosmology: observations — galaxies: evolution — galaxies: general — galaxies: clusters: individual (Abell 2125) — X-rays: general — X-rays: galaxies

1. Introduction

The structure of the universe is believed to have formed by clustering hierarchically from small to large scales. The outcome of this hierarchical formation process depends largely on

---

[1] Department of Astronomy, University of Massachusetts, Amherst, MA 01003

[2] National Radio Astronomy Observatory, P.O. Box O, Socorro, NM 87801, USA

[3] Gemini Observatory, Southern Operations Center, AURA, Casilla 603, La Serena, Chile

the interplay between galaxies and their environs. But how and where such galaxy/environ interactions primarily occur remain greatly uncertain (e.g., David et al. 1996; Wang & Ulmer 1997; Ponman et al. 1999; Fujita 2001; Balogh et al. 2002; Bekki et al. 2003).

We have identified a large-scale hierarchical complex (Fig. 1) that is well-suited for investigating the structure formation process and the galaxy/environment interactions. Revealed in a survey of 10 Butcher & Oemler clusters observed with the *ROSAT* PSPC (Wang & Ulmer 1997), this complex contains various X-ray-emitting features, which are associated with concentrations of optical and radio galaxies (Fig. 1; Wang, Connolly, & Brunner 1997a; Owen et al. 1999; Dwarakanath & Owen 1999). The overall optical galaxy concentration of the region was classified previously as a cluster Abell 2125 (richness 4). The *ROSAT* image and follow-up optical observations, however, have shown that the complex contains three well-defined X-ray bright clusters (Wang et al. 1997a). In addition, substantial amounts of unresolved low-surface brightness X-ray emission (LSBXE) are also present. The overall size of the complex is at least ~ 8 Mpc (the cosmological parameters, $H_0 = 71$ km s^{-1} Mpc^{-1}, $\Omega_{total} = 1$, and $\Omega_\Lambda = 0.73$ are adopted throughout the paper). The complex thus represents an X-ray-bright hierarchical filamentary superstructure, as predicted by numerical simulations of the structure formation (e.g., Cen & Ostriker 1996).

Interestingly, the complex also contains a distinct population of active galaxies. The blue galaxy fraction ($f_b \sim 20\%$) of Abell 2125 is the largest among rich clusters known at similar redshifts (e.g., Butcher et al. 1983; Wang & Ulmer 1997). In particular, 24 radio galaxies within the luminosity range of $10^{22} - 10^{23}$ W Hz^{-1} at 20 cm (Owen et al. 1999; Dwarakanath & Owen 1999) have been found in this field. But such a radio galaxy population is entirely absent in A2645, which is similarly rich in optical and has a similar redshift, but has both a much lower blue galaxy fraction ($\sim 5\%$) and a relaxed cluster X-ray morphology. This fact indicates that radio properties of galaxies are tightly linked to their environment.

We have obtained a deep *Chandra* observation that covers part of the Abell 2125 complex (Fig. 1) to characterize its detailed X-ray properties and to study the interplay between galaxies with their environs. The high spatial resolution of *Chandra* enables us to examine diffuse X-ray structures down to a scale of ~ 3.8 kpc ($\sim 1''$). In this paper, we concentrate on presenting the observation and the results on the detection of discrete sources and on the characterization of large-scale diffuse X-ray emission. Detailed analysis of the X-ray data in conjunction with observations in other wavelength bands is discussed elsewhere (e.g., Owen et al. 2003a,b)

2. Observation and data Analysis

The *Chandra* observation of Abell 2125 (Obs. ID. 2207) was taken on Aug. 24, 2001 for an exposure of 81.6 ks. The instrument ACIS-I was at the focal plane of the telescope and in the "VERY FAINT" mode, which allowed for a better software rejection of particle-induced events.

Our data calibration follows the same procedure detailed by Wang et al. (2003). Briefly, we reprocessed the level 1 (raw) event data to generate a new level 2 event file, using the *Chandra* Interactive Analysis of Observations software package (CIAO; version 2.3). The re-processing includes an improved absolute astrometry of the observation (nominally better than $\sim 0\farcs3$) and a correction for the charge transfer inefficiency of the CCDs. We further removed time intervals with significant background flares, or peaks with count rates $\gtrsim 3\sigma$ and/or a factor of $\gtrsim 1.2$ off the mean background level of the observation, using Maxim Markevitch's light-curve cleaning routine "lc_clean". This cleaning, together with a correction for the dead time of the observation, resulted in a net 80.5 ks exposure (livetime) for subsequent analysis.

We constructed broad band X-ray intensity images by flat-fielding count images with corresponding effective exposure maps, weighted with a power law of photon index 1.7. This flat-fielding corrected for telescope vignetting and bad pixels as well as the quantum efficiency variation of the instrument, including an observing date-dependent sensitivity degradation, which is particularly important at low energies $\lesssim 1.5$ keV.

We searched for X-ray sources in the three broad bands, (S) 0.5-2, (H) 2-8, and (B) 0.5-8 keV. A combination of source detection algorithms were applied: wavelet, sliding-box, and maximum likelihood centroid fitting. Source count rates were estimated within the 90% energy-encircled radius (EER) of the point spread function, which is off-axis dependent (Fig. 2). We removed a region of twice the 90% EER around each source to study diffuse X-ray emission. For visual presentation of smoothed diffuse X-ray intensity maps, we replaced the source-removed region with values estimated from data in surrounding bins.

To determine how many of our detected sources may be associated with the A2125 complex, we need to estimate the number of possible interlopers (e.g., background AGNs). We use the background source Log(N)–log(S) relation presented by Moretti et al. (2003 and references therein); here the source flux S is calculated in either the 0.5-2 keV band or the 2-10 keV band, assuming a power law of photon index of 1.4 and a foreground absorption 1.6×10^{20} cm^{-2}. The corresponding conversion from our B-band count rate to the fluxes in these two bands are 3.2 and 9.3×10^{-12} (erg cm^{-2} s^{-1})/(counts s^{-1}), respectively.

The sensitivity of our source detection depends on the size of the point spread function as well as the local background level and effective exposure, which all vary with position, especially with the off-axis angle of the observation (Fig. 3). This variation can seriously affect the number-flux relation of the detected sources, except for those with count rates $\gtrsim 10^{-3}$ counts s^{-1}. Furthermore, because of the limited counting statistics, many sources have very uncertain count rates. As a result of this large uncertainty, together with a typical steep number-flux distribution of background sources, more faint sources are expected to be scattered to fluxes above the detection limit than the other way around. This is similar to the Eddington bias in optical photometry (Hogg & Turner 1998) and is accounted for in our calculation of the expected interlopers in the field, according to the procedure detailed in Wang (2003).

In our diffuse X-ray spectral analysis, we take special care for the background subtraction. We estimated the background contribution in off-source regions (Fig. 2). To check the consistency of the background spectral properties in different regions, we compared the on- and off-source spectra extracted from the so-called blank-sky data[4]. With an effective livetime of 550 ks, the data were re-projected to mimic our observation, accounting approximately for both the cosmic X-ray background and the contribution from charged particle induced events. We found that a simple re-normalization of the off-source spectrum yielded statistically consistent on- and off-source blank-sky spectra. The re-normalization corresponded to a reduction of the livetime of the off-cluster spectrum by a factor of 1.16 ($\chi^2/d.o.f. = 360.7/328$). The renormalized off-source background of our observation was then used for the background subtraction in spectral analysis within XSPEC. For the LSBXE feature, the on- and off-source blank-sky spectra, are statistically consistent with each other ($\chi^2/d.o.f. = 482.5/450$). The best-fit normalization factor is 1.02, resulting only marginal improvement of the fit ($\chi^2/d.o.f. = 472.5/450$). We therefore, used the off-source spectrum from our observation without the normalization for the background subtraction of the LSBXE spectral analysis.

3. Results

3.1. Discrete X-ray Sources

Fig. 2 presents an overview of the ACIS-I image and the detected X-ray sources, whereas Table 1 lists the sources detected. Only sources with local false detection probability less than 10^{-7} are included. Various parameters are defined in the note to the table. In particular, the

---

[4] available at http://cxc.harvard.edu/contrib/maxim/acisbg/data/README

hardness ratios, compared with the models (Fig. 4) may be used to characterize the X-ray spectral properties of the sources.

Our detected sources are in the B-band count rate range of $0.1 - 12 \times 10^{-3}$ counts s^{-1}. The conversion from a count rate to an unabsorbed energy flux depends on the source spectrum (Fig. 5). A characteristic value of the conversion is $8{\times}10^{-12}$ (erg cm^{-2} s^{-1})/(counts s^{-1}) in the 0.5-8 keV band for a power law spectrum of photon index 2 and an absorbing-gas column density $N_H \sim 1 \times 10^{21}$ cm^{-2}. This conversion should be a good approximation (within a factor of 2) for $\lesssim 3 \times 10^{21}$ cm^{-2} (Fig. 5). The corresponding conversion to a source-frame luminosity in the same band is $\sim 1.4 \times 10^{45}$ (erg s^{-1})/(counts s^{-1}) at the distance of Abell 2125. The conversion to quantities in other bands can also be easily obtained. For example, the conversion to the luminosity in the 0.5-2 keV (or 2-10 keV) band is $\sim 0.86(0.99) \times 10^{45}$ (erg s^{-1})/(counts s^{-1}). With this conversion, one can estimate from the observed count rate the star formation rate as $\sim 2.2(2.0) \times 10^{-40} L_{0.5-2\mathrm{keV}}$ $(L_{2-10\mathrm{keV}})$ $\mathrm{M}_\odot$ yr^{-1} for starburst dominant galaxies (Ranalli, Comastri, & Setti 2003).

Fig. 6 compares the detected number-flux (count rate) distribution with the predicted, which includes the effects due to both the Eddington bias and the position-dependent sensitivity limit (§2). This direct comparison (without a fit) shows that the observed and predicted distributions are consistent with each other ($\chi^2 = 13.6$ for 10 bins). In the comparison, we have included only the 93 sources that are detected in the B band. Ten of these sources are found to be in positional coincidence with member galaxies of the A2125 complex and tend to show relative steep X-ray spectra, as indicated by the hardness ratios (Table 1) and by preferred detection in the S band (Owen et al. 2003a). One of the member sources has a count rate of 1.8×10^{-3} counts s^{-1}. All others have count rates in the range of $\sim 2.4 - 7.4 \times 10^{-4}$ counts s^{-1}, in which we see a slight excess of the observed number of sources above the predicted background contribution. The total predicted background source number is 85.6. Therefore, few (if any) of the remaining 84 sources detected in the B band are likely to be members of the complex.

There are other six X-ray sources that are detected only in the S band and one only in the H band (Table 1). These sources apparently have spectral characteristics that are quite different from the assumed spectrum for the average background sources and may or may not be associated with the complex.

The source detection reported here is optimized for point-like sources. Also we have used a quite conservative source detection threshold (i.e., a local false detection likelihood of 10^{-7}), which minimizes the global probability of including spurious sources in our list. With the priori positions of individual galaxies, one can lower the threshold for a positive detection of their X-ray counterparts (Owen et al. 2003a).

3.2. Diffuse X-ray Emission

We present in Fig. 7 adaptively smoothed ACIS-I intensity images. The presence of the large-scale diffuse X-ray emission is apparent. The overall morphology of the diffuse emission is very similar to that seen in Fig. 1, although part of the PSPC counts is clearly due to point-like sources detected now in the ACIS-I image. The diffuse emission is substantially softer than typical discrete sources. There are substructures in the diffuse X-ray emission on all scales, which may be more easily appreciated in images that are less heavily smoothed (e.g., Fig. 8).

The part of the large X-ray-emitting complex sampled by the ACIS-I observation consists of two relatively prominent concentrations: the X-ray core cluster Abell 2125 and the southwest LSBXE patch. The X-ray spectra of these two diffuse X-ray features are presented in Fig. 9 and the model spectral parameters are summarized in Table 2. We have obtained these results by assuming the mean optical redshift of the features to be $z = 0.247$, which is consistent with our direct fit to the X-ray spectral data: $z = 0.23(0.21 - 0.25)$ for Abell 2125 and $0.30(0.06 - 0.5)$ for the LSBXE. The 0.5-8 keV luminosities of the cluster and the LSBXE are 7.9 and 2.0×10^{43} ergs s^{-1} within the respective circular regions defined in Fig. 1. But these two features have significantly different temperatures and the abundances.

The diffuse X-ray surface brightness intensity of a relaxed cluster can typically be characterized by the standard β-model of the form (Cavaliere & Fusco-Femiano 1976):

$$I = I_o \left(1 + \frac{r^2}{r_c^2}\right)^{1/2-3\beta}, \tag{1}$$

where r is the off-center radius. However, the model gives a poor fit to the radial surface brightness intensity ($\chi^2/d.o.f. = 107/56$) and can be rejected at a confidence of $\sim 5\sigma$. Clearly, the morphology of the cluster is far from the axis-symmetric.

We thus characterize the morphological variation of the cluster with a series of ellipses on various scales (Fig. 10). Each ellipse is determined by the moments of the enclosed X-ray intensity distribution (e.g., Carter & Metcalfe 1980; Wang, Ulmer, & Lavery 1997b). We follow the iterative approach detailed in Wang et al. (1997b) to calculate the four parameters that define an ellipse: the center coordinates (R.A. and Dec. shifts relative to the aiming direction of the ACIS-I observation), ellipticity (ϵ), and orientation of the major axis (θ; north to east). The results obtained from the 0.5-8 keV band data are presented in Figs. 10 and 11. Note that the 90% statistical confidence error bars on different scales are not totally independent and thus overestimated, as the calculation of the moments uses all the data with each ellipse (Wang et a. 1997b). The most significant change of the ellipse parameters with the semi-major axis is the center R.A. position, which shifts by $\sim 10''$ from the inner region to outer region of cluster. The centroid of the cluster is offset to the northwest from the central triple of major galaxies, which coincide positionally with the three radio sources seen in the lower left panel of Fig. 7. This offset as well as the centroid shift and the elongation of the cluster morphology may be a manifestation of the underlying gravitational mass distribution. Galaxies in the field show another concentration about $1\rlap{.}'4$ to the northwest (Owen et al. 2003b). But the diffuse X-ray emission extends further to the north on larger scales (Fig. 10). This extension is reflected in the change of the ellipse orientation with the scale (Fig. 11, lower right panel).

Ignoring these small, though significant, morphological variations, we use the elliptical coordinates as defined by the ellipse parameters on the $2\rlap{.}'5$ scale (Table 3) to measure the surface brightness intensity profile as a function of the semi-major axis. A β-model fit to this profile obtained in the elliptical coordinates is acceptable (Fig. 12; Table 3) and may thus be considered as a characterization of the average large-scale properties of the cluster. We infer from the model the central electron density as $n_0 \sim 2.0 \times 10^{-3}$ cm^{-3}, assuming an oblate shape of the X-ray-emitting medium and the best-fit thermal plasma model (Table 2). The mean cooling time scale of the gas at the center of the cluster is then $t_{ICM} \sim 18$ Gyr, which is longer than the age of the Universe.

We have also conducted the same morphological characterization of the cluster in the 0.5-2 keV band. The 2-D ellipse fit in this band gives the ellipse parameters that are nearly identical to those in the 0.5-8 keV band, especially on the $2\rlap{.}'5$ scale. Except for the central intensity $I(0)$, the best-fit $\beta-$model parameters in the two bands are statistically consistent with each other, particularly with the consideration that β correlates with the core radius r_c in the parameter estimation. But the fit is much less satisfactory in the 0.5-2 keV band than in the 0.5-8 keV band.

3.3. Substructure in the X-ray Core Cluster

A careful inspection of the cluster images in various bands indicates that much of the deviation of the X-ray intensity distribution from the global elliptical β-model is caused by the presence of small-scale substructures, which are particularly apparent in the 0.5-2 keV band. For example, Fig. 7 lower panels clearly show photon energy-dependent features, which are strikingly associated with radio galaxies in the cluster core. Comparison with point-like sources in the vicinity indicates that these peaks are resolved.

To reveal details of such substructures in the cluster, we subtract the best-fit elliptical β-model from the 0.5-2 keV intensity map, which includes discrete sources. Fig. 13 shows the central region of the residual map. Clearly, there is an over-subtraction on the northwestern portion of the cluster core, which is due to the centroid shift with the scale, as discussed above.

The most apparent feature in this residual image is a "trail" apparently attached to Source 69, which has a radio galaxy counterpart C153 (or 00047, Owen et al. 2003a; Fig. 13; see also the lower panels of Fig. 7). This trail is only apparent in the 0.5-2 keV band and extends about $22''$ (corresponding to ~ 88 kpc at the distance of the cluster) from the galaxy to the northeast. A similar, though shorter, trail in the same direction is also seen in [OII] line emission (Owen et al. 2003b). With the limited counting statistics of the data, however, we cannot conclude that this apparent trail indeed represents a coherent diffuse X-ray structure. While the association of the first $\sim 10''$ high surface brightness portion of the trail with the galaxy appears convincing, the rest may become mixed up with other things, including possible weak discrete sources or statistical fluctuations. Nevertheless, it is interesting to consider the possibility that the entire trail is actually a coherent structure, originating from the galaxy and passing thorough the global centroid of the cluster.

Fig. 14 compares the surface brightness intensity across the trail. From this comparison, we estimate the average width of the trail as $\sim 4''$ (~ 16 kpc) and the total net count rate above the local background of ~ 0.01 counts s^{-1} arcmin^{-2} as $\sim 5.3(\pm 0.9) \times 10^{-4}$ counts s^{-1}. Although the very limited counting statistics does not allow for a tight constraint on the X-ray spectral properties, the complete absence of the trail in the 2-8 keV band (the lower panels of Fig. 7 and Fig. 14) suggests that the gas, if thermal, should have a temperature considerably lower than that of the average ICM. This lower temperature is also required to explain the enhancement of the X-ray emissivity, which is presumably due to the increased gas density to balance the thermal pressure in the surrounding ambient ICM. For a thermal plasma of a temperature ~ 0.5 keV, for example, the luminosity of the trail is $\sim 1 \times 10^{42}$ ergs s^{-1} in the 0.5-2 keV band. Furthermore, assuming that the gas is approximately uniformly distributed in the trail, we estimate the electron density as $\sim 1.0 \times 10^{-2}$ $\mathrm{cm}^{-3} \xi^{-0.5}$, where ξ is the gas metallicity in the solar units. The dependence on ξ assumes that lines from metals dominate the X-ray emission. If the trail gas is stripped from the galaxy and has $\xi \sim 1$, a pressure balance with the ambient ICM can then be achieved. If ξ is comparable to that of the ICM, however, the density, and therefore the pressure, would then be substantially larger. Reducing the temperature further may not help much since the radiation starts to move out of the energy band. Therefore, the metallicity in the trail appears higher than in the ICM. The total mass of the gas in the trail is $M_{trail} \sim 5 \times 10^{9} \xi^{-0.5} M_{\odot}$. Assuming the thermal pressure, the cooling time scale of the gas in the trail is about $t_{trail} \sim 0.8$ Gyr.

4. Discussion

Our *Chandra* results on the diffuse X-ray emission, now nearly free from significant discrete source contamination, are consistent with those obtained by Wang et al. (1997a) based on *ROSAT* PSPC data. In particular, we find that the LSBXE appears to be distinctly different from the ICM in the X-ray core cluster. Even the relatively prominent southwest patch of the LSBXE does not seem to be centrally peaked, as may be expected from a more-or-less virialized system such as a cluster or group of galaxies. It is possible, though, that the LSBXE represents concentrations of many small groups of galaxies. The average thermal temperature of the LSBXE patch is indeed consistent with that of typical groups (e.g., Helsdon & Ponman 2001). In this scenario, one would also expect a good correlation between X-ray-emitting peaks and elliptical galaxies, as is the case for nearby groups. We will investigate the scenario further in a later paper.

The heavy element abundance in the LSBXE appears to be substantially lower than that in the X-ray core cluster. The abundance may be underestimated in the LSBXE, if it contains multiple temperature components. But the existing data show no indication for this. The abundance enhancement of the X-ray core cluster relative to the LSBXE, if real, is probably due to processes such as ram-pressure stripping and/or tidal stripping of gas from galaxies.

Globally speaking, the LSBXE characterized here probably represents a local temperature and density enhancement of a large-scale gaseous structure, as indicated in the *ROSAT* PSPC image (Fig. 1), which is more sensitive to very soft X-rays ($\lesssim$ 0.5 keV) than the *Chandra* observation. Therefore, the whole complex, as a rich assembly of galaxies and gas, is apparently in the process to form a relaxed and luminous X-ray cluster.

We have now quantified the diffuse X-ray structure of the core cluster Abell 2125. In particular, the measured X-ray ellipticity of the cluster is the largest in the BO sample (Wang & Ulmer 1997). The elongation is not aligned with the overall orientation of the superstructure, however. This misalignment can take place, if the cluster represents an initial coalescence of subunits of comparable masses, which is consistent with the kinematics of the cluster galaxies (Miller et al. 2003). A merger of a rich cluster with small subclusters at a later stage of cluster evolution tends to produce a cluster elongation along a larger scale filament (West et al. 1995). The low temperature and luminosity of Abell 2125 (Table 2), relative to relaxed clusters of similar optical richness (e.g., Edge & Steward 1991), also indicate that the ICM has not yet been virialized and much of its energy may still in bulk motion.

The violent interactions of the active radio/optical galaxies with the ICM could naturally explain the diffuse X-ray substructures observed in the core of the cluster. The two most prominent soft X-ray enhancements in the lower right panel of Fig. 7 are associated with the radio galaxies C153 and 00057 (Figs. 7 lower panels and 13), which have radial velocities that are 1.67 $\times 10^3$ km s^{-1} and 1.32 $\times 10^3$ km s^{-1} off the mean of the core cluster (Miller et al. 2003). The associated soft X-ray enhancements may be due to the increased cooling and/or mixing between cold and hot gases because of the large ram-pressure around the galaxies. The soft X-ray trail following C153, in particular, shows the expected characteristics of the ram-pressure stripping of this galaxy. As predicted by Stevens et al. (1999) from numerical simulations, such a ram-pressure trail is more likely to be observed in cooler clusters such as Abell 2125 because of the longer stripping time-scale and the relatively larger tail-to-background X-ray intensity contrast. This ram-pressure stripping scenario is also consistent with the highly disturbed optical morphology of C153 at its southwest leading edge, as observed in a narrow band [OII] imaging. Such multi-wavelength observations and discussions on the properties of the galaxies will be presented in Owen et al. (2003b).

5. Summary

We have presented a deep *Chandra* ACIS-I observation of a large-scale hierarchical complex associated with Abell 2125. The superb spatial resolution and broad energy coverage of this observation have allowed us for the first time cleanly separate contributions from discrete sources and diffuse hot gas in the complex. The main results and conclusions we have obtained are summarized as follows:

- We detect 100 discrete sources with an on-axis flux limit of $\sim 8 \times 10^{-16}$ erg cm^{-2} s^{-1} in the 0.5-8 keV band. Ten of these sources have been identified to have optical counterparts spectroscopically confirmed as the A2125 complex members. The remaining sources are statistically consistent with being in the background to the complex, although a few of them, especially those with relatively steep X-ray spectral characteristics, may be associated with the complex. In the core cluster, soft and extended X-ray sources/peaks are associated with giant radio galaxies (the central triple and C153), indicating strong interactions between galaxies and the cluster environment.

- We characterize the global morphology of Abell 2125, using intensity isophote ellipses, which show significant centroid shifts with the spatial scale. An elliptical β-model gives a satisfactory fit to the surface brightness intensity profile in the 0.5-8 keV band, but not in the 0.5-2 keV band, in which morphological distortion due to substructures becomes more important.

- We confirm the detection of large amounts of low surface brightness diffuse X-ray emission in regions beyond the core cluster. In particular, the gas in the relatively prominent southwest patch has a mean thermal temperature of ~ 1 keV and a heavy element abundance of $\lesssim 9\%$ solar, substantially smaller than that in the ICM of the cluster. The low abundance suggests that the gas may represent the general IGM, falling to the cluster potential. The entire X-ray-emitting complex appears to be a manifestation of the large-scale hierarchical structure formation as predicted in theories.

We thank David Smith for his help in exporting the Log(N)–Log(S) analysis into XSPEC. This work was funded by NASA under the grants GO1-2126 and NAG5–8999.

REFERENCES

Balogh, M., et al. 2002, MNRAS, 337, 256

Bekki, K., Couch, W. J., & Shioya, Y. 2003, ApJ, 577, 651

Brinkmann et al. 1995, A&AS, 109, 147

Butcher, H. et al. 1983, ApJS, 52, 183

Dwarakanath, K. S., & Owen, F. N. 1999, AJ, 118, 625

Carter, D., & Metcalfe, N. 1980, MNRAS, 191, 325

Cavaliere, A., & Fusco-Femiano, R. 1976, A&A, 49, 137

Cen, R., & Ostriker, J. P. 1999, ApJ, 514, 1

David, L. P., Jones, C., & Forman, W. 1996, ApJ, 473, 692

Edge, A. C., & Stewart, G. C. 1991, MNRAS, 252, 414

Fujita, Y. 2001, ApJ, 550, 612

Helsdon, S. F., & Ponman, T. J. 2002, MNRAS, 325, 693

Hogg, D. W., & Turner, E. L. 1998, PASP, 110, 727

Miller et al. 2003, in preparation

Moretti, A., Campana, S., Lazzati, D., & Tagliaferri, G. 2003, A&A, 588, 696

Owen, F. N., et al. 1999, AJ, 118, 633

Owen, F. N., et al. 2003a, in preparation

Owen, F. N., et al. 2003b, in preparation

Ponman, T. J., et al. 1999, Nature, 397, 135

Ranalli, P., Comastri, A., & Setti, G. 2003, A&A, 399, 39

Stevens, I. R., Acreman, D. M., & Ponman, T. J. 1999, MNRAS, 310, 663

Wang, Q. D., Connolly, A., & Brunner, R. 1997a, ApJL, 487, 13

Wang, Q. D., Ulmer, M., & Lavery, R. J., 1997b, MNRAS, 292, 920

Wang, Q. D., & Ulmer, M. 1997, MNRAS, 290, 920

Wang, Q. D. 2003, in preparation

Wang, Q. D., Chaves, T., & Irwin, J. 2003, ApJ, Dec. 1 issue

West, M. J., Jones, C., & Forman, W. 1995, ApJL, 451, 5

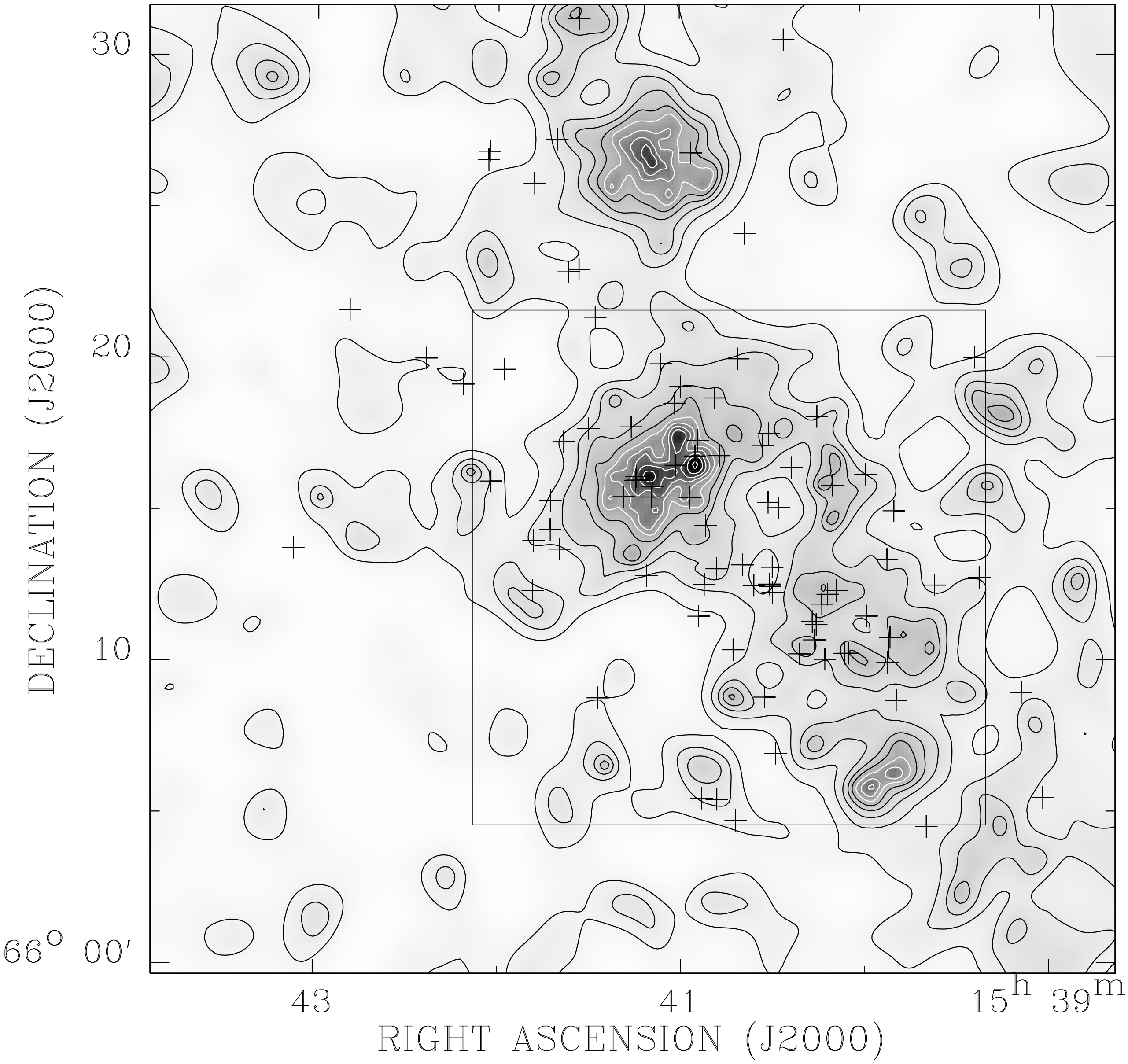

Fig. 1.— *ROSAT* PSPC X-ray image of Abell 2125 and its vicinity in the 0.5-2 keV band (Wang et al. 1997). Point-like X-ray sources detected in the image have been excised. Each contour is 50% (2σ) above its lower level. Spectroscopically confirmed, radio detected members of the Abell 2125 complex (Owen et al. 2003a) are marked by *pluses*. The box outlines the field covered by our *Chandra* ACIS-I observation (Fig. 2).

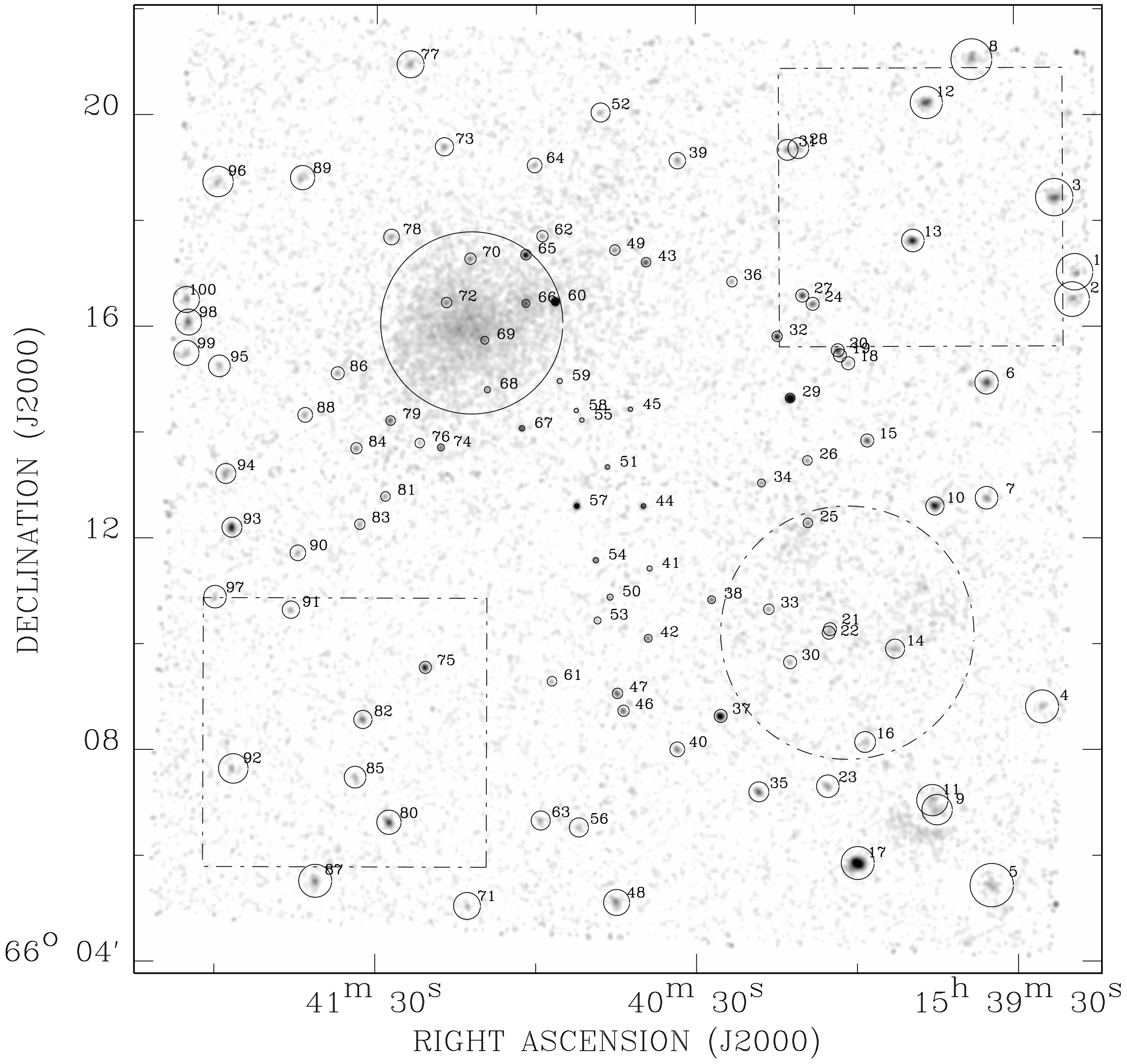

Fig. 2.— *Chandra* ACIS-I 0.5-8 keV image of the Abell 2125 field, smoothed with a Gaussian of FWHM equal to 3″ . The two large circles outline the on-source regions from which the spectral data of Abell 2125 and LSBXE are extracted, whereas the off-source background spectra are from the regions outlined by two squares. The small circles represent the regions removed for discrete sources, which are labeled as in Table 1.

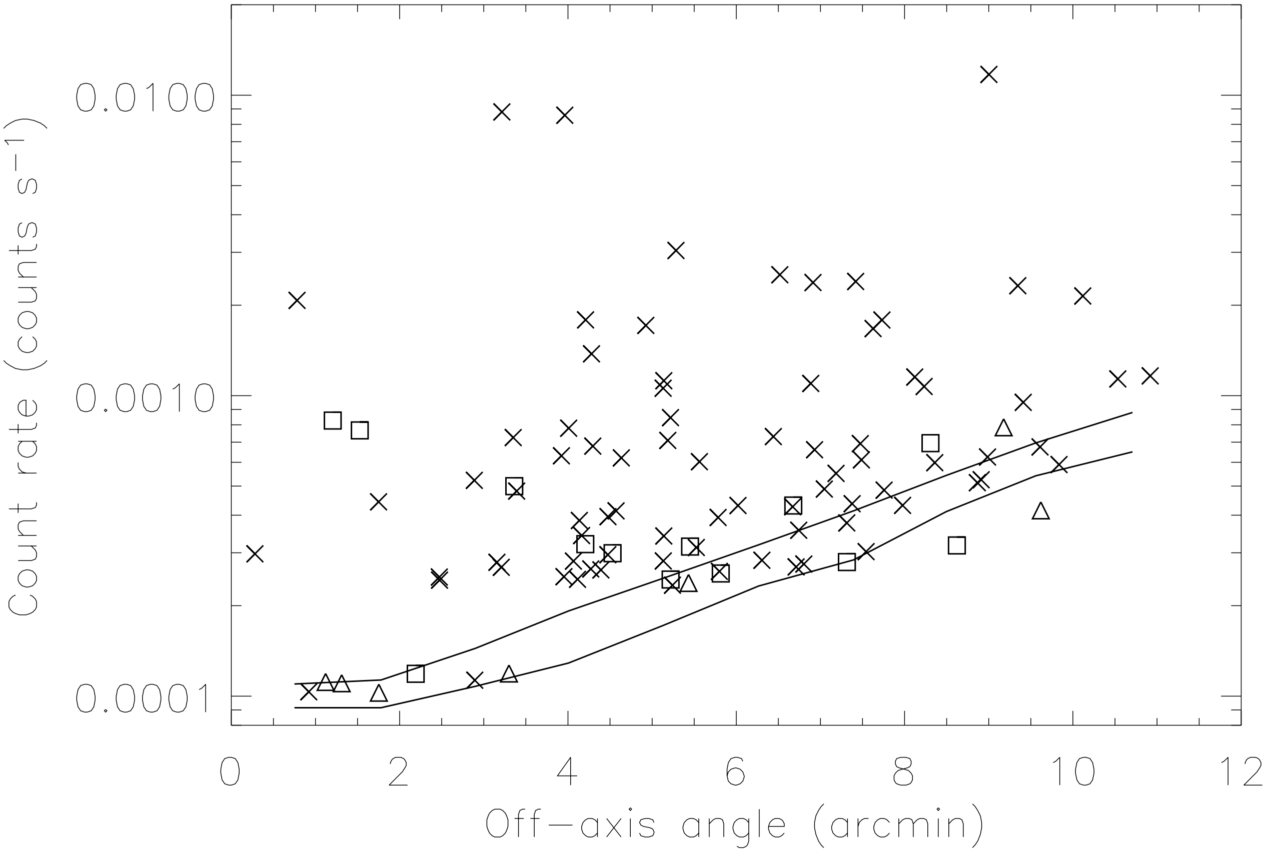

Fig. 3.— Source count rates vs. off-axis angle of the ACIS-I observation. Sources best detected in the B band are marked by *crosses*; sources detected best in other bands (but also in the B band) are marked by squares; and those not detected in the B band are represented by *triangles*. The upper and lower curves illustrate the expected B-band detection threshold, the azimuthally averaged and the lowest at each off-axis angle, respectively.

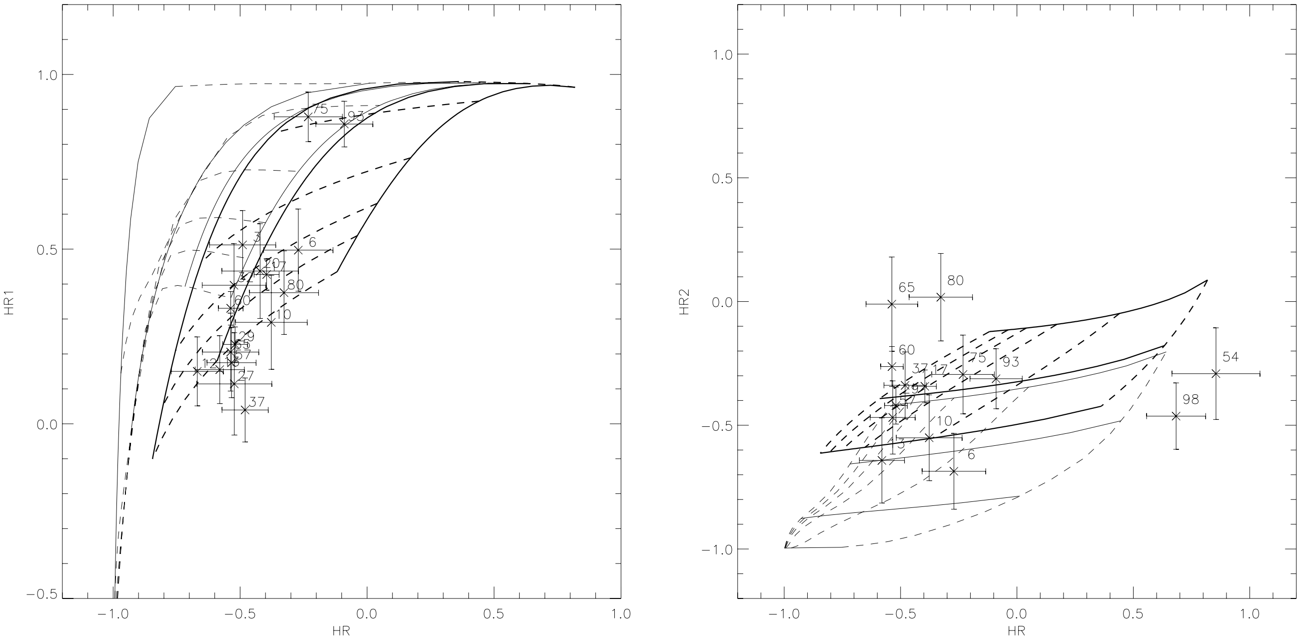

Fig. 4.— Color-color diagrams of X-ray sources with their generic numbers (Table 2) labeled. The hardness ratios (HR1, HR2, and HR) are defined in the notes to Table 1, and the error bars represent 1σ uncertainties. Also included in the plot are hardness-ratio models: the solid thick curves are for the power-law model with photon index equal to 3, 2, and 1, whereas the solid thin curves are for the thermal plasma with a temperature equal to 0.3, 1, 2, and 4 keV, from left to right in the left panel and from bottom to top in the right panel, respectively. The absorbing gas column densities are 1, 10, 20, 40, 100, and 300 $\times 10^{20}$ cm^{-2} (dashed curves from bottom to top in the left panel and from left to right in the right panel)

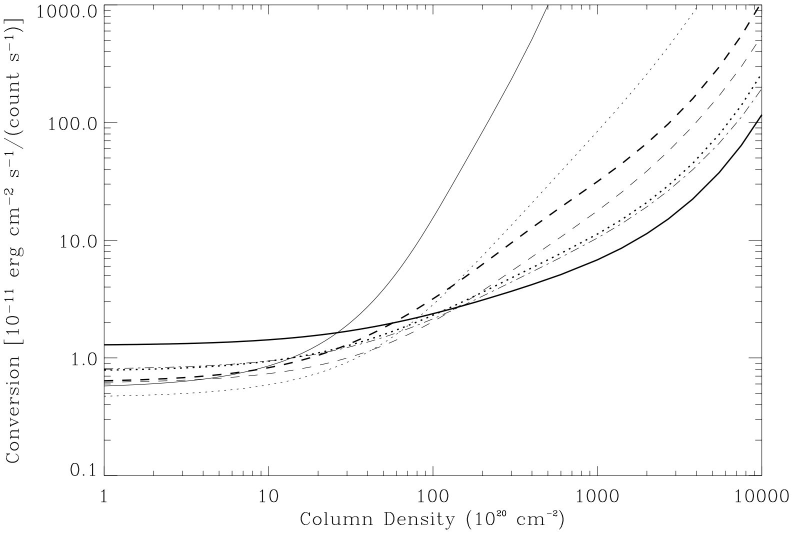

Fig. 5.— Conversion of an ACIS-I count rate to an energy flux in the 0.5-8 keV band for representative models: the thick curves are for the power-law model with a photon index equal to 1 (solid), 2 (dotted), and 3 (dashed), whereas the thin curves are for the thermal plasma with a temperature equal to 0.3 (solid), 1 (dotted), 2 (dashed), and 4 (dot-dashed) keV, respectively. The heavy element abundances are assumed to be solar for both the X-ray-emitting plasma and the absorbing gas.

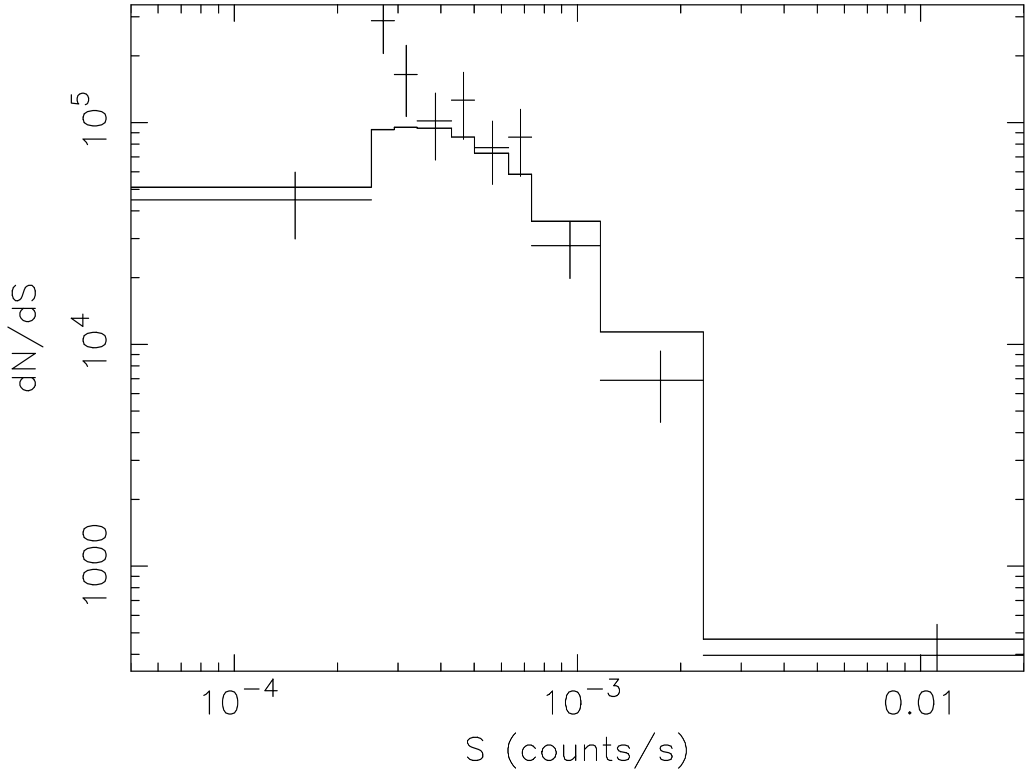

Fig. 6.— The observed source count rate distribution compared with the expected background contribution (histogram). Only the 93 sources detected in the B band (Table 1, Col. 9) are included in the comparison.

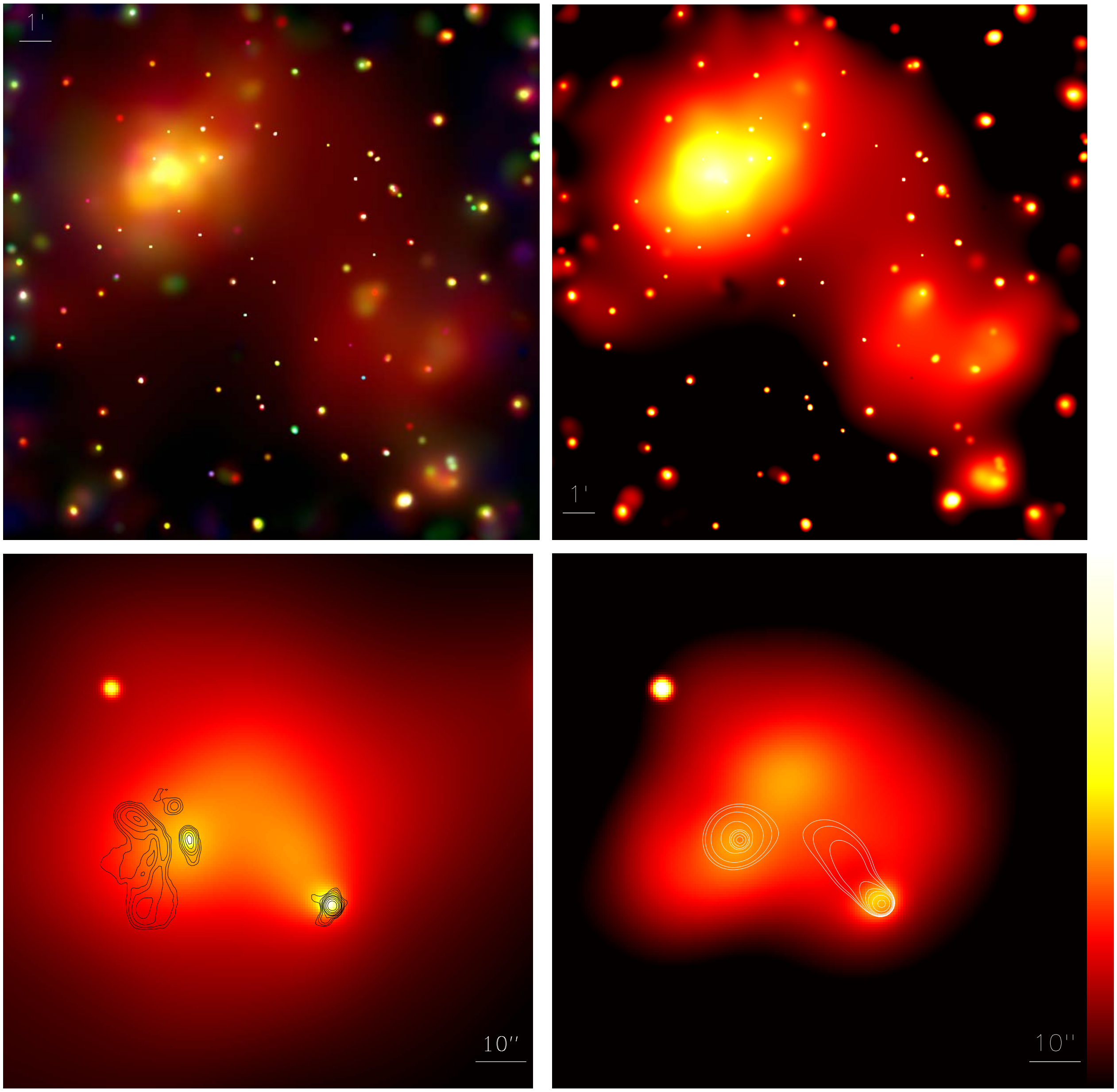

Fig. 7.— ACIS-I images of the Abell 2125 complex: Tri-color montage of X-ray intensities in three bands: (red) 0.5-2 keV, (green) 2-4 keV, and (blue) 4-8 keV (*Upper left panel*); Intensity in the 0.5-2 keV band (*Upper right panel*); Close-up of the Abell 2125 core in the 0.5-8 keV band with overlaid radio continuum intensity contours at 0.04, 0.08, 0.16, 0.32, 0.64, 0.96, 2, 4, and 8 mJy/beam (*Lower left panel*) and in the 2-8 keV band with the overlaid 0.5-2 keV intensity contours at 15.3, 15.5, 15.9, 16.5, 17.3, 18.3, 21.9, and 29.1×10^{-3} counts s^{-1} arcmin^{-2} (*Lower right panel*). The images are all adaptively smoothed with a 0.5-8 keV band S/N ratio of ~ 3, as defined in the CIAO routine CSMOOTH.

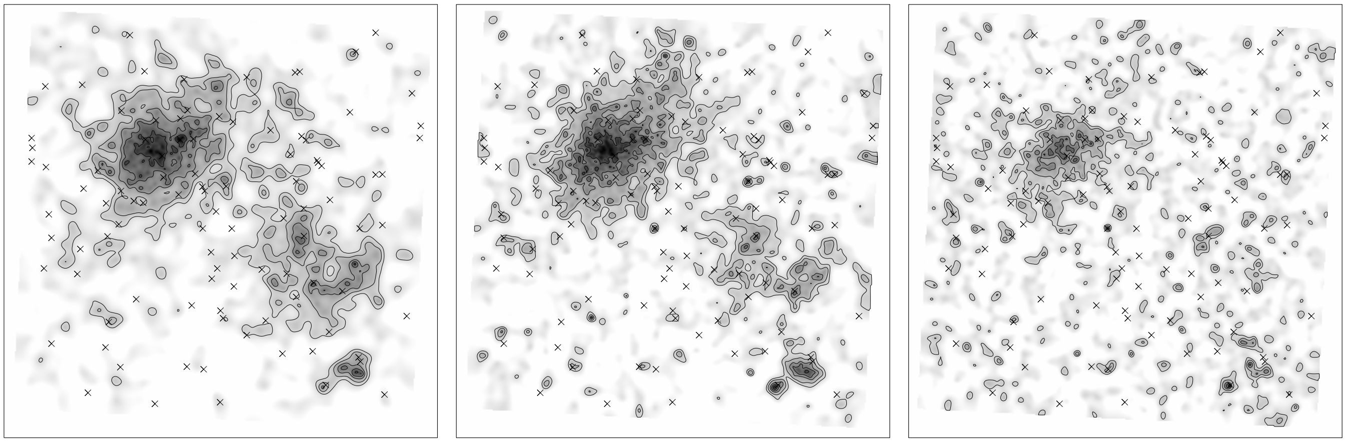

Fig. 8.— ACIS-I diffuse X-ray intensity images in three bands: 0.5-1 keV (left panel), 1-2 keV (middle panel), and 2-8 keV (right panel). The images are adaptively smoothed with a Gaussian, the size of which is adjusted to achieve a uniform count-to-noise ratio of ~ 6 across the field. Removed sources are marked with *crosses*.

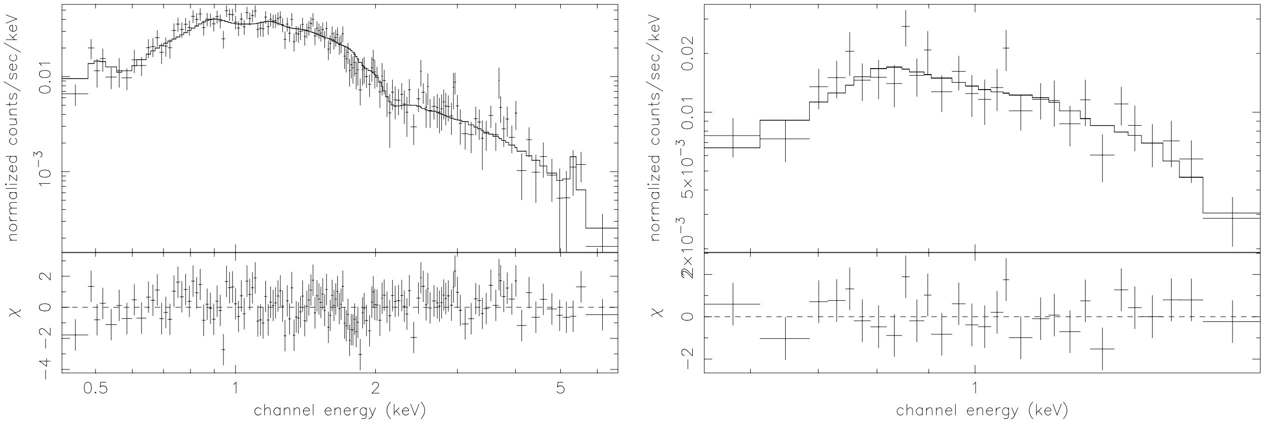

Fig. 9.— ACIS-I Spectra of the Abell 2125 core (left panel) and the LSBXE (right panel), together with the best-fit spectra models (Table 2).

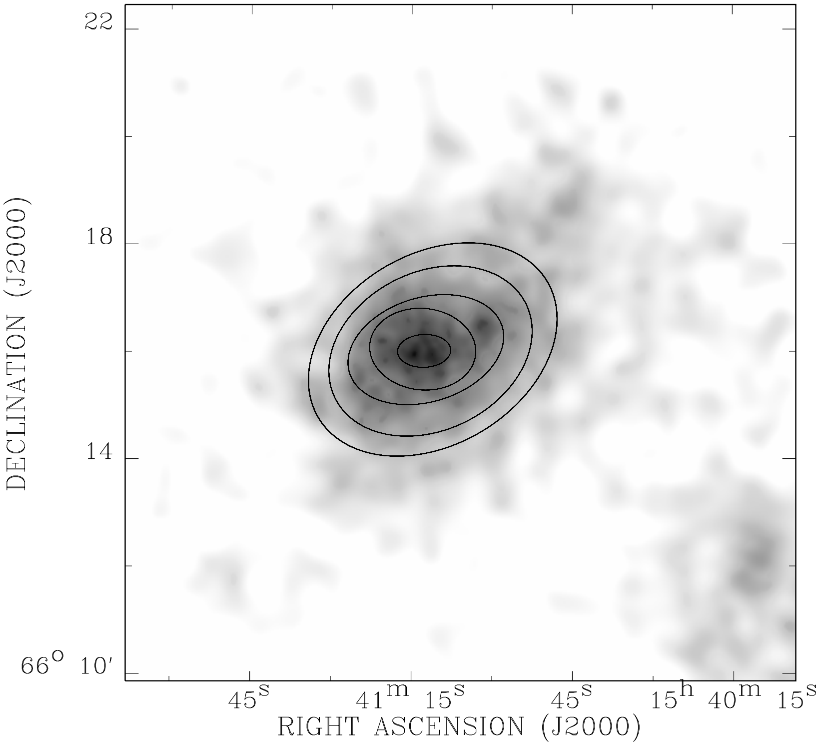

Fig. 10.— Characterization of the 2-D morphology of the 0.5-8 keV diffuse emission from the core cluster Abell 2125 with ellipses on evenly-spaced scales from 0′.5 - 2′.5. The gray-scale map is in the 0.5-2 keV band and is adaptively smoothed with a count-to-noise ratio of 6.

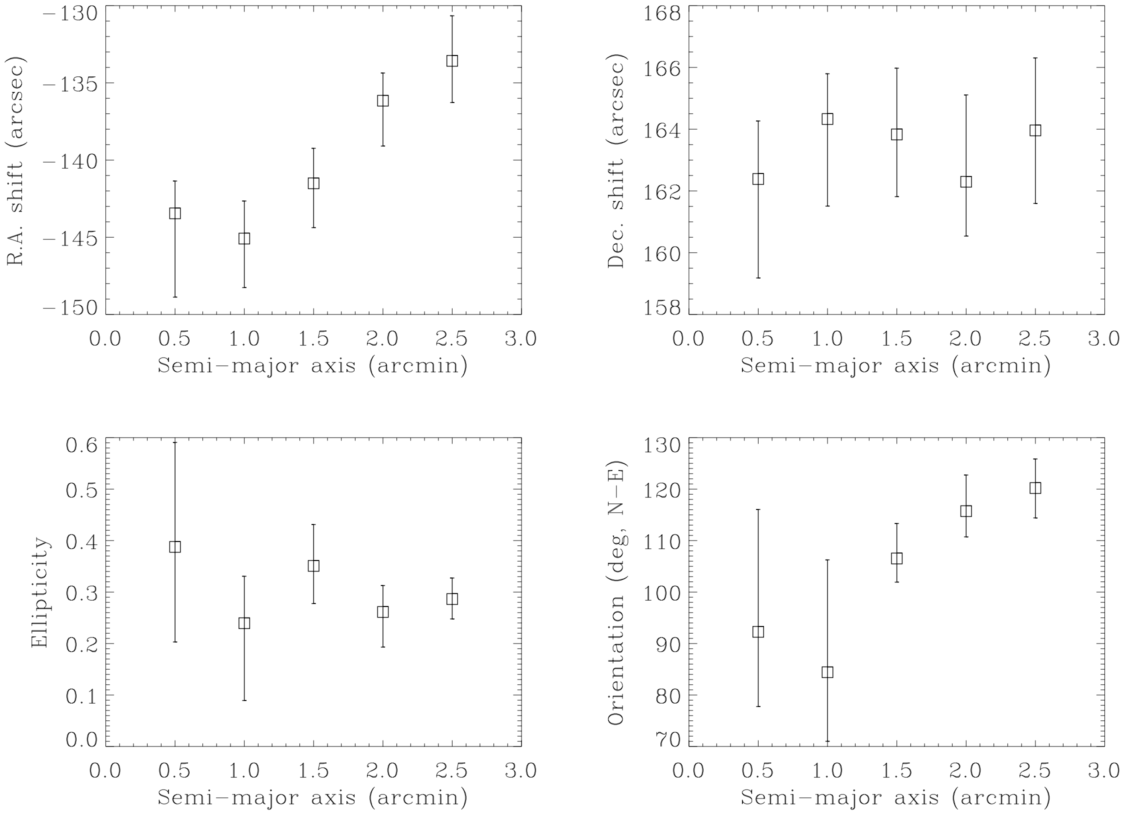

Fig. 11.— Center shifts, ellipticity, and orientation of the 0.5-8 keV intensity isophote ellipse as a function of semi-major axis. Error bars are at the 90% confidence level.

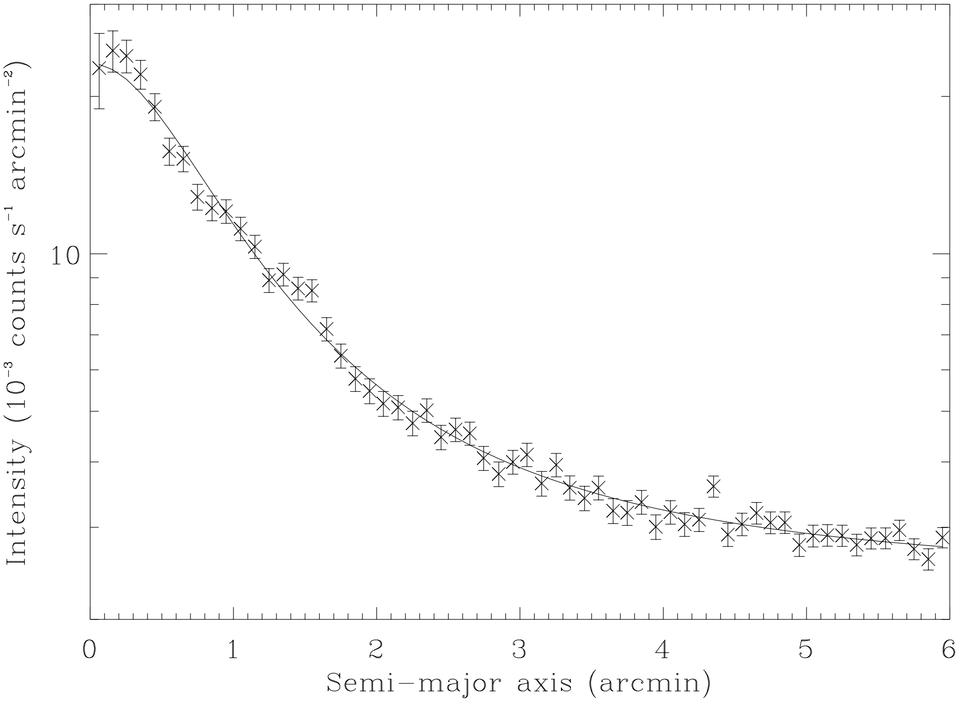

Fig. 12.— ACIS-I 0.5-8 keV surface brightness profile of Abell 2125 in the elliptical coordinates defined by the best-fit isophote ellipse on the scale of 5′ semi-major axis. The curve represents the best-fit β-model.

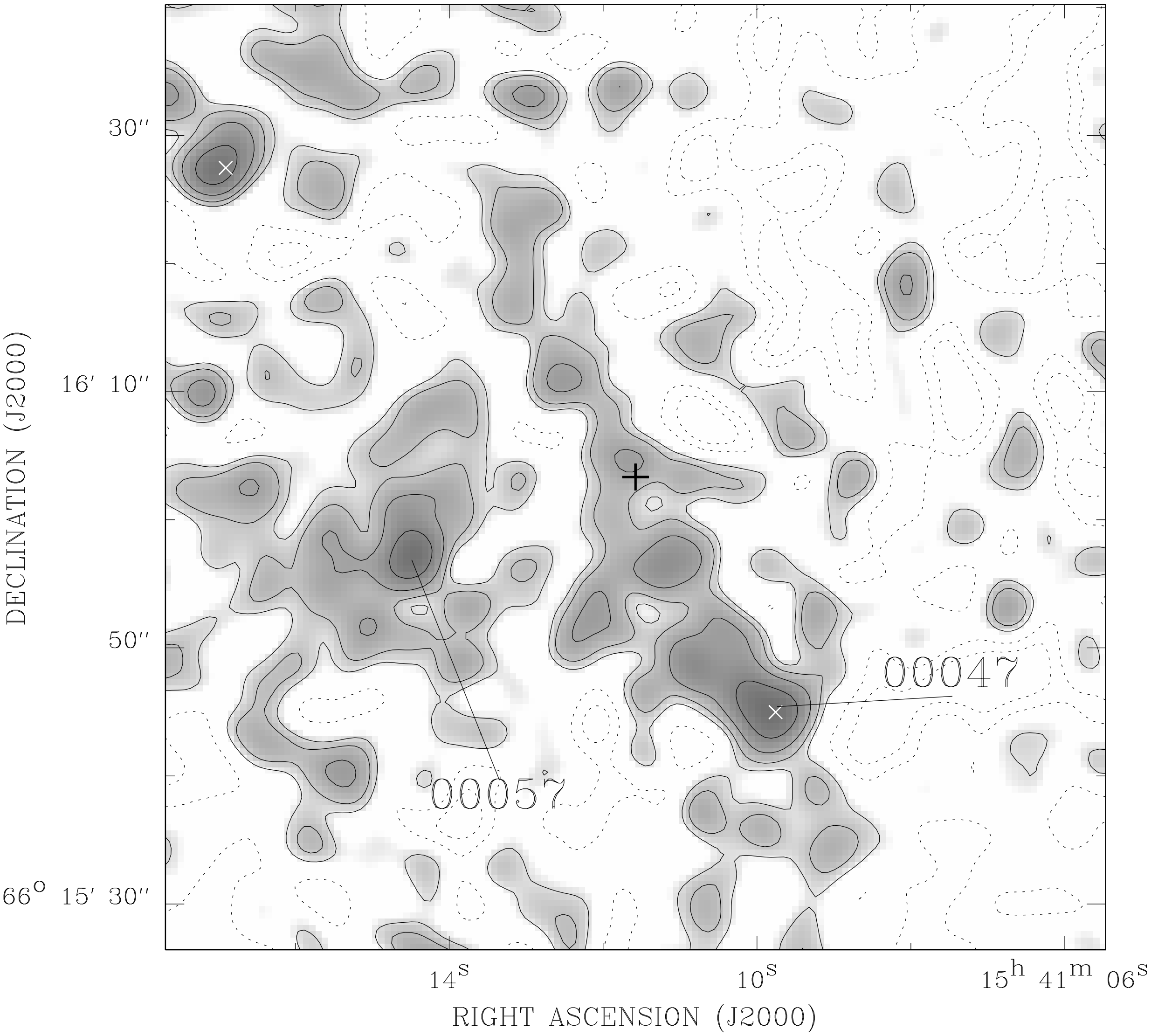

Fig. 13.— Residual map of the ACIS-I intensity in the central region of Abell 2125, after subtracting the best-fit elliptical β-model (Fig. 12; Table 3). The image is smoothed with a Gaussian of FWHM equal to 6″. The positive (solid) contours start at 6 $\times 10^{-3}$ counts s^{-1} arcmin^{-2} and increase by a factor of 2 successively, while the negative (dotted) contour are at (-6 and -12) $\times 10^{-3}$ counts s^{-1} arcmin^{-2}. The thick plus sign marks the adopted global cluster center (Table 3). Two key radio galaxies mentioned in the text are labeled (Owen et al. 2003b), and discrete X-ray source positions (Table 1) are also marked.

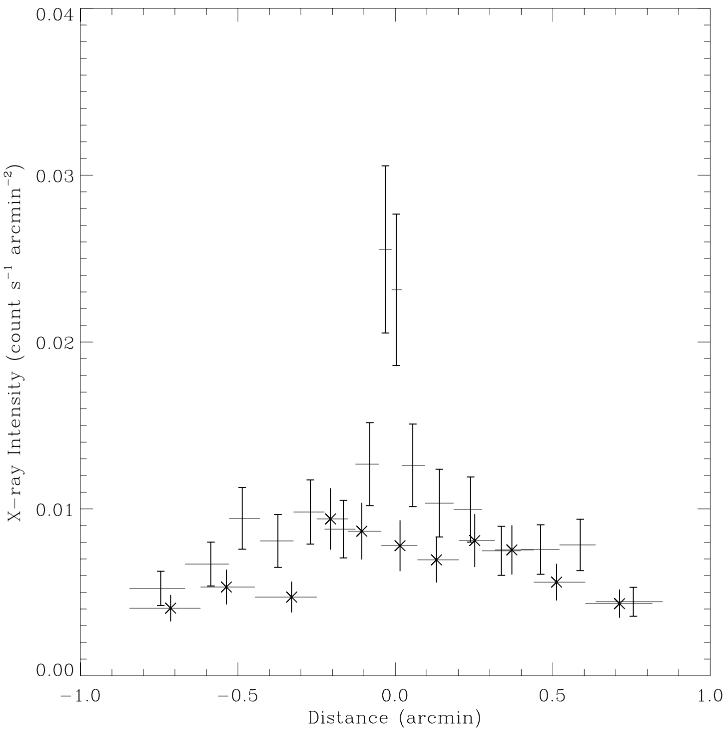

Fig. 14.— Average ACIS-I intensity distributions along a cut, which is 22” wide and perpendicular to the trail apparently following Source 69 or the optical/radio galaxy C153 (see also Fig. 7 lower panels and Fig. 13). The data points are obtained in two bands: 0.5-1.5 keV and 1.5-4 keV (marked by “x”). The vertical error bars are at 1σ, whereas the horizontal bars represent the off-trail distance ranges of the data points.

Table 1. *Chandra* Source List

Source (1)	CXOU Name (2)	δ_x ($''$) (3)	log(P) (4)	CR (cts ks^{-1}) (5)	HR (6)	HR1 (7)	HR2 (8)	Flag (9)
1	J153918.89+661700.8	2.2	−12.7	0.59 ± 0.15	–	–	–	B
2	J153919.36+661629.6	2.1	−13.7	0.68 ± 0.14	–	–	–	B, S
3	J153922.59+661825.4	1.0	−20.0	2.15 ± 0.21	−0.49 ± 0.13	0.51 ± 0.10	–	B, S, H
4	J153925.48+660848.2	3.1	−8.3	0.42 ± 0.12	–	–	–	S
5	J153935.02+660525.8	1.7	−20.0	1.16 ± 0.17	–	−0.09 ± 0.18	–	B, S, H
6	J153935.49+661455.9	0.7	−16.5	1.67 ± 0.17	−0.27 ± 0.14	0.50 ± 0.12	−0.69 ± 0.15	B, S, H
7	J153935.61+661244.8	1.7	−12.2	0.69 ± 0.16	–	–	–	B, S
8	J153938.08+662102.7	1.8	−15.7	1.14 ± 0.19	–	0.12 ± 0.19	–	B, S, H
9	J153945.15+660651.7	1.9	−8.2	0.78 ± 0.15	–	–	–	S
10	J153945.28+661236.1	0.5	−16.9	2.53 ± 0.28	−0.38 ± 0.14	0.29 ± 0.13	−0.55 ± 0.17	B, S, H
11	J153946.05+660702.4	1.6	−12.9	0.62 ± 0.13	–	–	–	B, H
12	J153946.67+662013.4	0.9	−15.6	2.32 ± 0.21	−0.67 ± 0.10	0.15 ± 0.10	–	B, S, H
13	J153949.30+661737.1	0.6	−15.6	2.40 ± 0.21	−0.58 ± 0.10	0.16 ± 0.10	−0.64 ± 0.17	B, S, H
14	J153952.87+660954.0	1.1	−12.6	0.43 ± 0.10	–	–	–	B, S
15	J153957.97+661350.4	0.7	−16.7	0.85 ± 0.13	–	−0.12 ± 0.16	–	B, S
16	J153958.54+660808.5	1.6	−11.7	0.28 ± 0.09	–	–	–	S, B
17	J154000.02+660551.2	0.3	−15.9	11.72 ± 0.46	−0.40 ± 0.05	0.43 ± 0.04	−0.34 ± 0.07	B, S, H
18	J154001.51+661518.2	1.0	−11.4	0.24 ± 0.07	–	–	–	S, B
19	J154003.00+661527.1	1.1	−16.8	0.34 ± 0.08	–	–	–	B, S
20	J154003.44+661532.8	0.6	−16.8	1.12 ± 0.13	−0.42 ± 0.15	0.44 ± 0.14	–	B, S, H
21	J154005.03+661016.6	1.2	−8.0	0.24 ± 0.07	–	–	–	S
22	J154005.29+661012.5	0.9	−14.5	0.31 ± 0.08	–	–	–	S, B
23	J154005.55+660718.5	1.3	−16.0	0.61 ± 0.11	–	–	–	B, H, S
24	J154008.12+661625.5	0.6	−16.3	0.71 ± 0.11	–	0.25 ± 0.18	–	B, S
25	J154009.13+661217.0	0.7	−16.3	0.32 ± 0.08	–	–	–	S, B
26	J154009.20+661328.0	0.8	−15.9	0.28 ± 0.07	–	–	–	B, H
27	J154010.07+661635.2	0.6	−16.3	1.06 ± 0.13	−0.52 ± 0.15	0.11 ± 0.15	–	B, S, H
28	J154010.75+661922.5	1.1	−15.9	0.55 ± 0.10	–	–	–	B, S
29	J154012.39+661438.8	0.1	−16.1	8.57 ± 0.37	−0.52 ± 0.05	0.23 ± 0.05	−0.42 ± 0.07	B, S, H
30	J154012.55+660939.3	1.3	−10.3	0.23 ± 0.07	–	–	–	B, H
31	J154012.77+661920.3	1.2	−20.0	0.49 ± 0.10	–	–	–	B, H
32	J154014.83+661548.7	0.4	−15.9	1.38 ± 0.15	−0.52 ± 0.13	0.40 ± 0.12	–	B, S, H
33	J154016.54+661039.6	0.7	−13.4	0.27 ± 0.07	–	–	–	B, S
34	J154017.83+661302.7	1.0	−14.5	0.27 ± 0.08	–	–	–	B, S, H
35	J154018.45+660712.6	0.7	−16.4	1.10 ± 0.14	–	−0.03 ± 0.15	–	B, S, H
36	J154023.34+661651.1	1.1	−13.5	0.26 ± 0.07	–	–	–	B, H, S
37	J154025.58+660838.4	0.3	−16.6	3.04 ± 0.23	−0.48 ± 0.09	0.04 ± 0.09	−0.34 ± 0.13	B, S, H
38	J154027.18+661050.6	0.4	−20.0	0.50 ± 0.09	–	0.34 ± 0.20	–	S, B
39	J154033.52+661908.4	1.0	−15.8	0.43 ± 0.09	–	–	–	B, H
40	J154033.64+660800.7	0.7	−20.0	0.60 ± 0.10	–	–	−0.20 ± 0.18	B, H, S
41	J154038.84+661125.8	0.7	−12.5	0.12 ± 0.05	–	–	–	S, B
42	J154039.11+661006.8	0.5	−20.0	0.48 ± 0.09	–	–	–	B, H, S
43	J154039.46+661713.1	0.6	−16.5	0.78 ± 0.11	–	0.61 ± 0.14	–	B, S, H
44	J154039.99+661236.6	0.2	−20.0	0.83 ± 0.11	–	0.41 ± 0.15	–	S, B, H
45	J154042.41+661426.2	1.7	−8.0	0.11 ± 0.07	–	–	–	S
46	J154043.73+660844.5	0.7	−16.0	0.62 ± 0.11	–	–	–	B, S, H
47	J154044.85+660904.1	0.8	−20.0	0.68 ± 0.16	–	–	–	B, S
48	J154045.02+660507.1	1.2	−20.0	1.07 ± 0.17	–	–	–	B, S, H

Table 1—Continued

Source (1)	CXOU Name (2)	δ_x ($''$) (3)	log(P) (4)	CR (cts ks^{-1}) (5)	HR (6)	HR1 (7)	HR2 (8)	Flag (9)
49	J154045.34+661727.2	0.7	−16.1	0.38 ± 0.08	–	–	–	B, S, H
50	J154046.22+661053.3	0.8	−11.6	0.25 ± 0.09	–	–	–	B, S
51	J154046.73+661320.9	0.3	−16.3	0.30 ± 0.07	–	–	–	B, S, H
52	J154048.03+662002.9	2.0	−7.1	0.27 ± 0.08	–	–	–	B
53	J154048.55+661026.8	0.8	−8.1	0.11 ± 0.05	–	–	–	B, H
54	J154048.86+661135.4	0.3	−16.7	0.44 ± 0.09	0.86 ± 0.19	–	−0.29 ± 0.19	B, H
55	J154051.54+661414.2	0.5	−7.7	0.10 ± 0.04	–	–	–	B
56	J154052.03+660632.4	1.7	−7.6	0.28 ± 0.08	–	–	–	B, S
57	J154052.44+661236.9	0.1	−20.0	2.08 ± 0.18	−0.53 ± 0.10	0.17 ± 0.10	−0.47 ± 0.15	B, S, H
58	J154052.56+661424.9	0.5	−9.9	0.11 ± 0.04	–	–	–	S
59	J154055.69+661458.6	1.3	−7.8	0.10 ± 0.05	–	–	–	S
60	J154056.45+661628.6	0.1	−20.0	8.80 ± 0.37	−0.54 ± 0.05	0.33 ± 0.05	−0.26 ± 0.08	B, S, H
61	J154057.13+660917.8	0.7	−14.2	0.24 ± 0.07	–	–	–	B, S
62	J154058.93+661742.6	0.9	−11.8	0.30 ± 0.08	–	–	–	B, S
63	J154059.21+660640.0	1.3	−12.5	0.36 ± 0.09	–	–	–	B
64	J154100.39+661903.0	1.5	−11.5	0.26 ± 0.08	–	–	–	S, B
65	J154102.01+661721.4	0.3	−20.0	1.79 ± 0.17	−0.54 ± 0.11	0.21 ± 0.11	−0.01 ± 0.19	B, S, H
66	J154102.04+661626.5	0.3	−20.0	0.73 ± 0.12	–	−0.24 ± 0.16	–	B, S
67	J154102.76+661404.7	0.2	−17.8	0.77 ± 0.11	–	0.48 ± 0.16	–	S, B, H
68	J154109.25+661448.7	0.5	−14.1	0.24 ± 0.06	–	–	–	B, S
69	J154109.79+661544.7	0.5	−9.6	0.28 ± 0.07	–	–	–	B, S
70	J154112.48+661717.0	0.9	−20.0	0.41 ± 0.09	–	–	–	B, S
71	J154112.90+660502.8	2.0	−10.6	0.32 ± 0.10	–	–	–	S, B
72	J154116.94+661627.2	0.7	−9.5	0.34 ± 0.09	–	–	–	B
73	J154117.43+661923.8	1.4	−20.0	0.43 ± 0.09	–	–	–	S, B
74	J154117.92+661343.0	0.4	−17.0	0.52 ± 0.09	–	–	–	B, S, H
75	J154120.83+660933.7	0.4	−20.0	1.71 ± 0.18	−0.23 ± 0.13	0.88 ± 0.07	−0.29 ± 0.16	B, S, H
76	J154121.93+661347.9	1.0	−7.2	0.12 ± 0.05	–	–	–	H
77	J154123.79+662057.2	1.5	−15.4	0.60 ± 0.12	–	–	–	B, H
78	J154127.33+661741.7	1.5	−10.7	0.39 ± 0.10	–	–	–	B, S
79	J154127.43+661413.6	0.6	−16.8	0.63 ± 0.11	–	0.79 ± 0.15	–	B, S, H
80	J154127.51+660637.6	0.8	−16.1	1.78 ± 0.18	−0.33 ± 0.14	0.38 ± 0.12	0.02 ± 0.18	B, S, H
81	J154128.35+661247.5	0.7	−13.5	0.25 ± 0.07	–	–	–	B, S
82	J154132.46+660834.5	1.1	−15.7	0.73 ± 0.14	–	0.75 ± 0.15	–	B, S
83	J154133.15+661215.8	0.9	−15.1	0.30 ± 0.08	–	–	–	S, B
84	J154133.78+661341.8	0.8	−16.4	0.40 ± 0.08	–	–	–	B, S
85	J154133.86+660728.6	1.3	−15.0	0.44 ± 0.10	–	–	–	B, S
86	J154137.33+661506.7	1.1	−9.2	0.28 ± 0.08	–	–	–	B, S
87	J154141.29+660531.0	1.5	−20.0	0.95 ± 0.15	–	0.35 ± 0.17	–	B, S
88	J154143.47+661419.4	1.0	−15.0	0.31 ± 0.08	–	–	–	B, S
89	J154144.13+661848.7	1.3	−14.6	0.48 ± 0.10	–	0.83 ± 0.17	–	B, S
90	J154144.72+661143.0	1.6	−9.5	0.26 ± 0.07	–	–	–	B, S
91	J154145.99+661038.3	1.6	−9.7	0.28 ± 0.08	–	–	–	B, S
92	J154156.70+660738.9	1.9	−11.3	0.51 ± 0.12	–	–	–	B, S
93	J154157.12+661211.6	0.5	−15.7	2.38 ± 0.20	−0.09 ± 0.11	0.86 ± 0.07	−0.31 ± 0.12	B, S, H
94	J154158.26+661312.5	1.1	−20.0	0.66 ± 0.14	–	–	–	B, S
95	J154159.60+661514.9	1.4	−12.9	0.38 ± 0.09	–	–	–	B, S
96	J154200.02+661843.8	2.0	−11.1	0.53 ± 0.11	–	–	–	B, H

Table 1—Continued

Source (1)	CXOU Name (2)	δ_x ($''$) (3)	log(P) (4)	CR (cts ks^{-1}) (5)	HR (6)	HR1 (7)	HR2 (8)	Flag (9)
97	J154200.21+661053.0	1.8	-7.8	0.30 ± 0.09	–	–	–	B, H
98	J154205.44+661604.4	1.0	-20.0	1.15 ± 0.15	0.68 ± 0.13	–	-0.46 ± 0.13	B, H, S
99	J154205.78+661529.1	1.9	-10.3	0.43 ± 0.11	–	–	–	B, H
100	J154205.82+661629.8	1.6	-16.1	0.69 ± 0.15	–	0.54 ± 0.20	–	S, B

Note. — Column (1): Generic source number. (2): *Chandra* X-ray Observatory (unregistered) source name, following the *Chandra* naming convention and the IAU Recommendation for Nomenclature (e.g., http://cdsweb.u-strasbg.fr/iau-spec.html). (3): Position uncertainty (1σ) in units of arcsec. (4): The false detection probability P that the detected number of counts may result from the Poisson fluctuation of the local background within the detection aperture [log(P) smaller than -20.0 is set to -20.0]. (5): On-axis (exposure-corrected) source count rate in the 0.5-8 keV band. (6-8): The hardness ratios defined as HR = (H − S)/(H + S), HR1 = (S2 − S1)/S, and HR2 = (H2 − H1)/H, where S1, S2, H1, and H2 are the net source count rates in the 0.5–1, 1–2, 2–4, and 4–8 keV bands, respectively, while S and H represent the sums, S1+S2 and H1+H2. The hardness ratios are calculated only for sources with individual signal-to-noise ratios greater than 4 in the broad band (B=S+H), and only the values with uncertainties less than 0.2 are included. (9): The label "B", "S", or "H" mark the band in which a source is detected; the detection with the most accurate position, as adopted in Column (2), is marked first.

Table 2. Results of Spectral fits

Parameter	Cluster	LSBXE
Best-fit χ^2/d.o.f.	155/151	22/25
Column Density (10^{20} cm^{-2}) .	1.6($\lesssim$ 3.7)	0.1 ($\lesssim$ 10)
Abundance (10^{-2} solar)	0.24(0.12-0.39)	0.03($\lesssim$ 0.09)
Temperature (keV)	3.2(2.8-3.7)	0.98(0.71-1.2)
Integrated EM (10^{10} cm^{-5}) . .	5.8(5.3-6.4)	4.0(3.1-7.6)
$f_{0.4-7\mathrm{keV}}$(10^{-13} erg s^{-1} cm^{-2})	4.3	1.1

Note. — The uncertainty ranges of the parameters are included in the parentheses and are all at the 90% confidence. The integrated emission measure is defined as $1/4\pi \int_\Omega \mathrm{EM} d\Omega$, where the integration is over a solid angle over which the data are collected and EM = $\int n_e^2 dr$ with n_e being the electron density (all units in cgs).

Table 3. β-model fits to the Cluster Surface Brightness Profiles

Parameter	0.5-8 keV band	0.5-2 keV band
Center R.A. (J2000)	$15^h41^m11\rlap{.}''3$	$15^h41^m11\rlap{.}''6$
Center Dec. (J2000)	$66^\circ16'2''$	$66^\circ16'3''$
Ellipticity	0.29	0.29
Position angle (°)	123	120
β	0.52 (0.47-0.58)	0.62 (0.56-0.73)
r_c (′)	0.910 (0.773-1.08)	1.20(1.04-1.46)
(kpc)	210(178 - 248)	276 (240-336)
$I_o(10^{-2}$ cts s^{-1} arcmin$^{-2})$	2.1(1.9-2.2)	1.5(1.3-1.6)
$\chi^2/d.o.f$	66/56	96/56

Note. — Uncertainties in parameter values, as presented in parentheses, are all at the 90% confidence level.